






Two-gap s_{\pm} -wave superconductivity at an oxide interfaceG. Singh ^{1,2,5,*} G. Venditti,^{3,4,*} G. Saiz,¹ G. Herranz ⁵ F. Sánchez ⁵ A. Jouan,¹ C. Feuillet-Palma,¹ J. Lesueur,¹ M. Grilli ^{3,4} S. Caprara ^{3,4,†} and N. Bergeal^{1,‡}¹Laboratoire de Physique et d'Étude des Matériaux, ESPCI Paris, PSL University, CNRS, Sorbonne Université, 10 rue Vauquelin 75005 Paris, France²Quantum Device Physics Laboratory, Department of Microtechnology and Nanoscience MC2, Chalmers University of Technology, SE 412 96 Gothenburg, Sweden³Institute for Complex Systems (ISC-CNR), UOS Sapienza, Piazzale A. Moro 5, I-00185 Roma, Italy⁴Dipartimento di Fisica Università di Roma "La Sapienza", Piazzale A. Moro 5, I-00185 Roma, Italy⁵Institut de Ciència de Materials de Barcelona (ICMAB-CSIC), Campus de la UAB, 08193 Bellaterra, Catalonia, Spain

(Received 23 December 2020; revised 27 January 2022; accepted 31 January 2022; published 22 February 2022)

After half a century of debate, superconductivity in doped SrTiO₃ has come to the fore again with the discovery of interfacial superconductivity in the LaAlO₃/SrTiO₃ heterostructures. While these interfaces share the interesting properties of bulk SrTiO₃, quantum confinement generates a complex band structure involving bands with different orbital symmetries whose occupancy is tunable by electrostatic doping. Multigap superconductivity has been predicted to emerge in LaAlO₃/SrTiO₃ at large doping, with a Bose-Einstein condensation character at the Lifshitz transition. In this article, we report on the measurement of the upper critical magnetic field H_{c2} of superconducting (110)-oriented LaAlO₃/SrTiO₃ heterostructures and evidence a two-gap superconducting regime at high doping. Our results are quantitatively explained by a theoretical model based on the formation of an unconventional s_{\pm} -wave superconducting state with a repulsive coupling between the two condensates.

DOI: [10.1103/PhysRevB.105.064512](https://doi.org/10.1103/PhysRevB.105.064512)**I. INTRODUCTION**

In a superconductor, the formation of Cooper pairs involving two electrons in a spin-singlet state ($k \uparrow, -k \downarrow$), opens a gap in the excitation spectrum. When several bands cross the Fermi level, multigap superconductivity can take place and favor exotic superconducting orders that have no equivalent in a single-band picture. For instance, the s_{\pm} -wave superconducting state, characterized by a π phase difference between two superconducting order parameters is realized in iron-based superconductors [1–3]. In two-band superconductors, the constraint on the spin state is also lifted and spin-triplet s -wave superconductivity was predicted in the presence of strong Rashba spin-orbit coupling [4], leading to topological superconductivity in some cases [5]. Over the last decades, an increasing number of materials (e.g., MgB₂ [6], iron-based superconductors [7–10], and heavy fermions [11,12]) were found to be multiband superconductors, providing fertile ground to test theoretical predictions beyond conventional superconductivity.

In this context, n -doped-SrTiO₃, the first oxide superconductor to be discovered, can be regarded as a singular case [13]. Depending on the electron density, one, two, or three bands can be filled while superconductivity extends over more than three orders of magnitude in carrier concentration [14]. In 1980, Binnig *et al.* reported a double-gap

structure in Nb-doped bulk SrTiO₃ for a carrier density $n_{3D} \simeq 5 \times 10^{19} \text{ cm}^{-3}$ [15]. However, while multiband occupancy in SrTiO₃ is now firmly established experimentally [14], recent tunneling spectroscopy and microwave conductivity measurements were consistent with single-gap superconductivity, in apparent contradiction to the seminal experiment [16,17]. Half a century after its discovery, the origin of superconductivity in SrTiO₃ is still a matter of intense debate. The recent development of superconducting heterostructures, such as LaAlO₃/SrTiO₃ [18] or LaTiO₃/SrTiO₃ [19], has renewed interest in this material and triggered important efforts to elucidate the pairing mechanism behind the superconductivity [20–22].

In oxide interfaces, electrons are trapped in a quantum well that extends into SrTiO₃ and form a two-dimensional electron gas (2-DEG). They occupy a set of two-dimensional (2D) subbands resulting from the splitting of Ti t_{2g} bands [23–26]. With respect to the bulk material case, crystal orientation [27–30] and electrostatic gating [31–33] offer extra degrees of freedom to explore multiband superconductivity in SrTiO₃-based 2-DEG. Here, we study the temperature dependence of the upper critical field $H_{c2}(T)$ of the (110)-oriented LaAlO₃/SrTiO₃ interface as a function of gate-tunable carrier density. Depending on doping, we observe two distinct behaviors that, consistent with the Hall effect, correspond to single-gap and two-gap superconductivity. A two-band superconductivity model based on the diffusive Usadel equations is used to fit experimental data, extract the superconducting gaps and the coupling parameters for both bands. Surprisingly, the superconducting critical temperature T_c is suppressed at the transition between the two regimes. We ascribe this behavior to a pair-breaking interband scattering in the presence of a

*These authors contributed equally to this work.

†sergio.caprara@roma1.infn.it

‡nicolas.bergeal@espci.fr

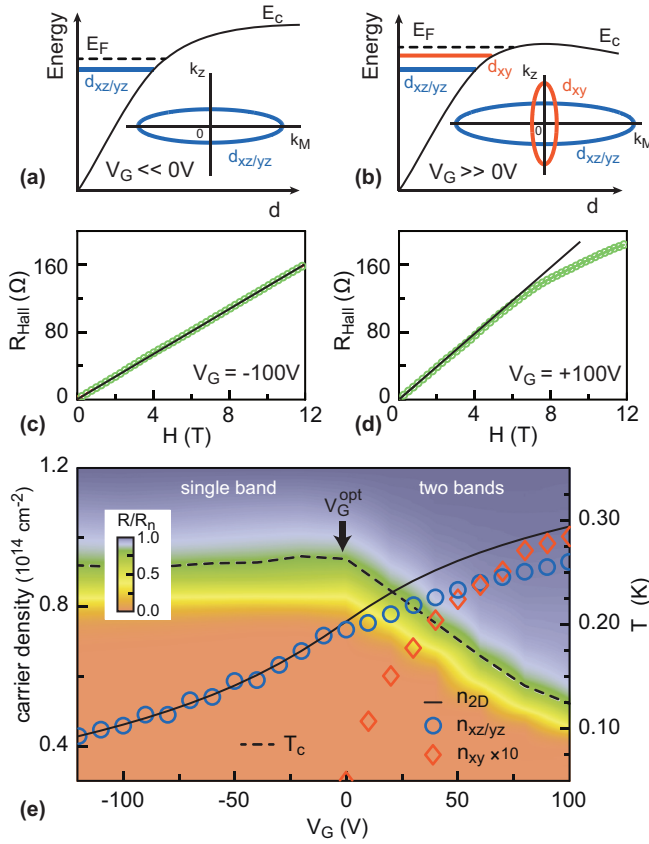


FIG. 1. Sketch of the band structure in the quantum well of (a) (110)-oriented LaAlO₃/SrTiO₃ oxide interfaces at low doping for $V_G < 0$ and (b) high doping for $V_G > 0$. The sketches show the confinement energy E_C in SrTiO₃ as a function of the distance to the interface d , the Fermi energy (E_F) and the position of the different t_{2g} bands at the Γ point. Insets show the Fermi contours in the $[k_z, (001)]$, k_M ($[1-10]$) plane. Hall resistance (opened symbols) as a function of magnetic field measured at (c) $V_G = -100$ V and (d) $V_G = +100$ V. The black full line is a linear fit of the low field Hall resistance. (e) Sheet resistance normalized by its value R_n at $T = 0.45$ K in color scale as a function of V_G and T (right axis). The black dashed line corresponds to T_c (right axis) which is defined as 80% of R_n . Carrier density in the $d_{xz/yz}$ ($n_{xz/yz}$) and d_{xy} (n_{xy} multiplied by a factor of 10) bands, and total carrier density (n_{2D}), extracted from the Hall effect and the gate capacitance measurements with a two-carrier model (Appendix A), plotted as a function of V_G at $T = 3$ K (left axis).

repulsive coupling between the two condensates [34,35] and derive a model for s_{\pm} -wave superconductivity in the presence of disorder that quantitatively explains our results. Finally, we discuss the signature of a Bose-Einstein condensation (BEC) in the vicinity of the Lifshitz transition.

II. SUPERCONDUCTING PHASE DIAGRAM AND HALL EFFECT

The samples considered here were obtained by pulsed laser deposition of ten-monolayers-thick LaAlO₃ films on (110)-oriented SrTiO₃ substrates [27,33]. Figures 1(a) and 1(b) show a sketch of the band structure inside the interfacial quantum

well and the associated Fermi contours for two different values of electrostatic doping [27]. In this crystal orientation, the band hierarchy is reversed with respect to the conventional (001)-orientation: at the Γ point, the d_{xy} band has higher energy than the degenerate $d_{xz/yz}$ band [27,33]. After growth, the LaAlO₃/SrTiO₃ structure is mounted on the mixing chamber plate of a dilution refrigerator and cooled down to 3 K. The gate voltage V_G is first increased to a maximum value $V_G^{\max} = +100$ V, to suppress hysteresis and ensure that transport measurements will be fully reversible in gate voltage [36].

Two transport regimes are clearly identified in the Hall effect since the two bands have different electronic mobilities [33]. While for negative gate voltages the Hall resistance R_{Hall} shows a linear variation with magnetic field [Fig. 1(c)], associated with filling the low-energy degenerate $d_{xz/yz}$ band, for positive gate voltages, R_{Hall} exhibits a non-linearity [Fig. 1(d)], which is consistent with the additional filling of the d_{xy} band. Figure 1(e) shows the gate evolution of the carrier density in each band, $n_{xz/yz}$ and n_{xy} , and the total carrier density n_{2D} , deduced from a two-carrier analysis of the Hall effect combined with gate capacitance measurements [37]. The procedure to extract both the mobilities and the carrier densities is detailed in Appendix A. The d_{xy} band, which starts to be populated at $V_G \simeq 0$ V, accommodates less than 10% of the total carrier density n_{2D} at maximum doping. At lower temperature, the 2-DEG undergoes a superconducting transition to a zero-resistance state in the entire doping range [Fig. 1(e)]. The superconducting T_c clearly identifies two distinct regions in gate voltage: an underdoped (UD) regime $[-120$ V, 0 V] where T_c is almost constant and an overdoped (OD) regime $[0$ V, $+100$ V] where a sharp decrease in T_c is observed. The transition between the two regimes occurs at an optimal doping voltage $V_G^{\text{opt}} \simeq 0$ V, which suggests that the OD region is associated with the two-band transport regime observed by the Hall effect in the normal state.

III. CRITICAL MAGNETIC FIELDS

To investigate multiband superconductivity, we measured the sheet resistance of the 2-DEG under a magnetic field H perpendicular to the interface plane for each gate voltage. Figures 2(a) and 2(b) show examples of the temperature dependence of the sheet resistance R for different critical fields and two gate voltages: $V_G = -100$ V in the UD regime and $V_G = +60$ V in the OD one. In the following, we define the critical magnetic field H_{c2} as the value of H at which the sheet resistance recovers 80% of the normal state value. Note that the main conclusions of our analysis are insensitive to this criterion. Figure 2(c) shows the normalized critical field $h_{c2} = H_{c2}(T)/H_{c2}(T=0)$ plotted as a function of the reduced temperature $t = T/T_c$. The graph highlights two distinct gate voltage regimes. In the UD, all curves collapse onto a single curve, with a temperature dependence that is consistent with the Werthamer-Helfand-Hohenberg (WHH) model for single-gap superconductivity, considering only the orbital pair breaking [38]. In the OD region, the curvature in the $h_{c2}(t)$ curves changes from downward to upward. This is emphasized by the sign change in the second derivative of h_{c2} that occurs at $V_G^{\text{opt}} \simeq 0$ V [Fig. 2(e), inset]. The upward curvature

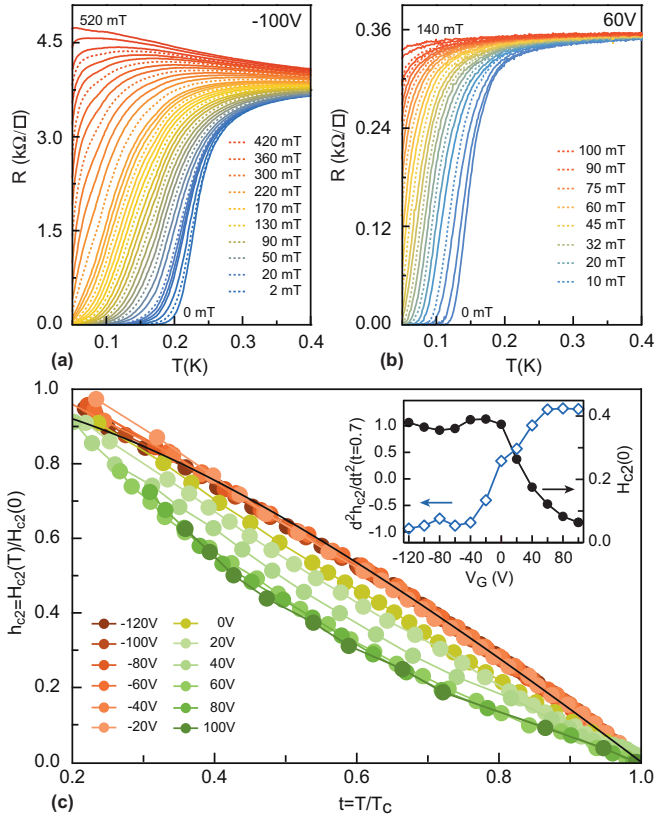


FIG. 2. Sheet resistance of the 2-DEG as a function of temperature under constant magnetic field applied perpendicular to the interface plane for (a) $V_G = -100$ V and (b) $V_G = 60$ V. Measurements were performed with the current aligned along the (001) direction. (c) Normalized critical magnetic field $h_c = \frac{H_c(T)}{H_c(0)}$ as a function of the reduced temperature $t = \frac{T}{T_c}$ for different gate voltages. The critical magnetic field H_{c2} is defined as the value of H for which the sheet resistance recovers 80% of the normal state value. The black line corresponds to the WHH model for single gap superconductivity [38]. Inset: $\frac{d^2 h_c}{dt^2}$ as a function of V_G (left axis) that emphasizes the change in curvature of $h_c(t)$ curves in the OD regime at $t = 0.7$. The critical field extrapolated at $T = 0$ K is shown on the right axis.

in the OD regime is characteristic of multiband superconductors, as already discussed in other materials (e.g., MgB_2 [39] and Fe-based superconductors [40]) [41]. A similar behavior has sometimes been attributed to the presence of nodes in the superconducting gap, but this later possibility does not apply to $\text{LaAlO}_3/\text{SrTiO}_3$, for which superfluid stiffness measurements and tunneling spectroscopy show a nodeless gap structure [42–44]. This nodeless pairing might seem at odds with the presence of a substantial spin-orbit interaction in $\text{LaAlO}_3/\text{SrTiO}_3$ interfaces [37,45–47], which is expected to induce a mixing of singlet-triplet pairing [48]. However, the triplet pairing necessarily involves a p -wave-like character of the pair wave function, which is much more sensitive to disorder than the s -wave component. Since the interfaces investigated in this work are characterized by moderate/strong disorder, the triplet component due to spin-orbit coupling will be substantially suppressed, thereby accounting for the nodeless character of pairing in these systems. In addition, we also

note that, in contrast to the (001)-oriented case, the Rashba spin-orbit coupling in (110)-oriented $\text{LaAlO}_3/\text{SrTiO}_3$ 2-DEG was found to be rather gate-independent, which is inconsistent with the sudden change in behavior observed in our system at optimal doping [33]. We therefore focus our analysis on the s -wave component only thereby neglecting the effect of the spin-orbit coupling on the superconducting phase. The results on the critical magnetic field shown in Fig. 2(a) are consistent with recent microwave measurements of superfluid stiffness, which suggest that a single-gap to two-gap superconductivity transition takes place at optimal doping [49]. Multiband superconductivity was also predicted in the conventional (001)-oriented $\text{LaAlO}_3/\text{SrTiO}_3$ heterostructures [35,50] whose band structure differs from that of the present case. However, it remains to be demonstrated experimentally in this orientation.

We analyzed more quantitatively the $h_{c2}(T)$ curves by following the approach proposed by Gurevich, in which linearized two-band Usadel equations are solved as a function of both the external magnetic field and the temperature [51]. We introduce the intraband ($\lambda_{11(22)}$) and interband ($\lambda_{12(21)}$) dimensionless coupling constants that determine the superconducting critical temperature

$$T_c \simeq 1.14 T_D \exp[(\lambda_0 - \lambda_{11} - \lambda_{22})/2(\lambda_{11}\lambda_{22} - \lambda_{12}\lambda_{21})], \quad (1)$$

where $\lambda_0 = [(\lambda_{11} - \lambda_{22})^2 + 4\lambda_{12}\lambda_{21}]^{1/2}$ and T_D is the Debye temperature. The interband coupling constants must satisfy the symmetry relation $\lambda_{12}N_1 = \lambda_{21}N_2$, where $N_{1(2)}$ is the density of states in band 1 (band 2). The critical field H_{c2} is obtained numerically as the root of the equation

$$a_0 \left[\ln \frac{T}{T_c} + U(g) \right] \left[\ln \frac{T}{T_c} + U(\eta g) \right] + a_1 \left[\ln \frac{T}{T_c} + U(g) \right] + a_2 \left[\ln \frac{T}{T_c} + U(\eta g) \right] = 0, \quad (2)$$

where $U(x) = \psi(\frac{1}{2} + x) - \psi(\frac{1}{2})$, $\psi(x)$ is the digamma function, $g = H_{c2}D_1/2\phi_0T$ is the reduced critical magnetic field, and $\eta = D_2/D_1$ is the ratio of the diffusivity in each band (the subscripts 1 and 2 refer to the $d_{xz,yz}$ and d_{xy} bands, respectively). The coefficients a_i are related to the coupling constants, $a_0 = 2(\lambda_{11}\lambda_{22} - \lambda_{12}\lambda_{21})/\lambda_0$, $a_1 = 1 + (\lambda_{11} - \lambda_{22})/\lambda_0$, and $a_2 = 1 - (\lambda_{11} - \lambda_{22})/\lambda_0$. The superconducting gaps $\Delta_{1(2)}$ are then deduced from the coupling constants as described in Appendix B.

Experimental data were fitted (solid lines) with Eq. (2), using the dimensionless coupling constants and the diffusivities as free parameters. Figure 3 shows the results of the fitting procedure for a selection of gate voltages spanning both doping regimes. In the UD regime, we assume that superconductivity only takes place in the low energy $d_{xz/yz}$ band, which is formally equivalent to the WHH model. As seen in Figs. 3(a) to 3(f), a good agreement between the model and experimental data is obtained for a coupling constant $\lambda_{11} \approx 0.135$ [inset Fig. 4(a)]. An almost gate-independent superconducting gap $\Delta_{xz/yz} \simeq 40 \mu\text{V}$ is deduced [Fig. 4(a)], whose value is consistent with tunneling spectroscopy measurements on (001)- $\text{LaAlO}_3/\text{SrTiO}_3$ heterostructures of equivalent

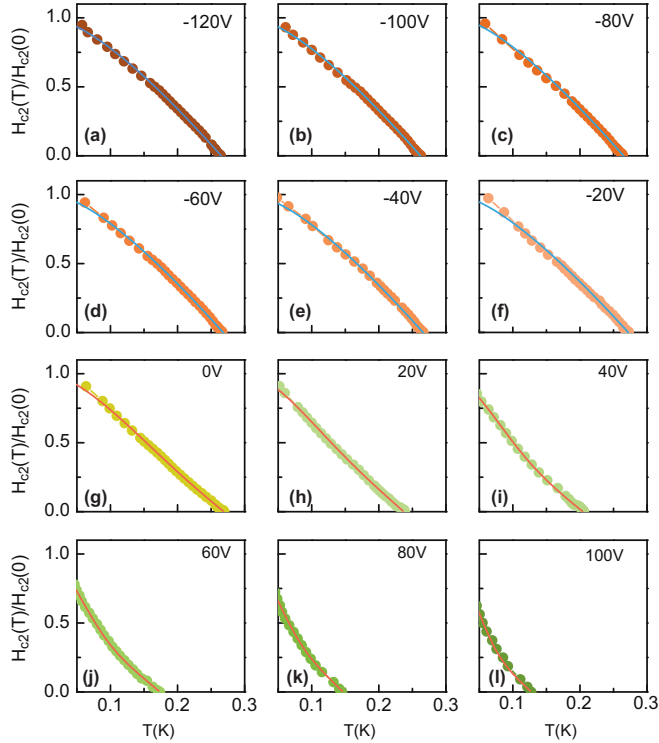


FIG. 3. Normalized critical field $h_c = H_{c2}(T)/H_{c2}(0)$ as function of temperature (symbols) fitted by the solutions of Eq. (2) (full lines) for a selection of gate voltages spanning both the (a)–(f) UD and (g)–(l) OD regimes. In panels (a)–(f), corresponding to the single gap regime, we assume $\lambda_{22} = \lambda_{12} = \lambda_{21} = 0$.

T_c [44] and superfluid density ones in the (110) orientation [49]. In the OD regime, the d_{xy} band is also populated and h_{c2} curves are well described by a two-gap model [Figs. 3(g) to 3(l)]. The coupling constant λ_{22} in the high-energy band is found to be slightly larger than λ_{11} [inset Fig. 4(a)], and so is the second gap associated with Δ_{xy} compared to [Fig. 4(a)]. In the entire doping regime the average interband coupling constant $\lambda_c = \sqrt{\lambda_{12}\lambda_{21}}$ is much smaller than λ_{11} and λ_{22} , showing that intraband coupling dominates [Fig. 4(a), inset]. Note that the fitting procedure only gives access to the product of the interband coupling constants $\lambda_{12}\lambda_{21}$ and not to their relative sign. The experimental values of the coupling constants determined here are consistent with that previously found in superfluid density measurements [49].

In Fig. 4(b), we compare the gate dependence of the diffusion coefficients $D_{xz,yz}$ and D_{xy} obtained from the Usadel fits to that extracted from a simple two-carrier analysis of the Hall effect and gate capacitance data (see Appendix B). A qualitative agreement is observed both in the single-band and the two-band regime, showing the consistency of the results between the normal state and the superconducting one. In our analysis, the suppression of the gap in the two-band regime is reproduced by introducing an artificial decrease of the intraband coupling constants which is not physical [Fig. 4(a)]. As we will see in the following, a more detailed microscopic model that includes the effect of disorder is needed to fully explain our data.

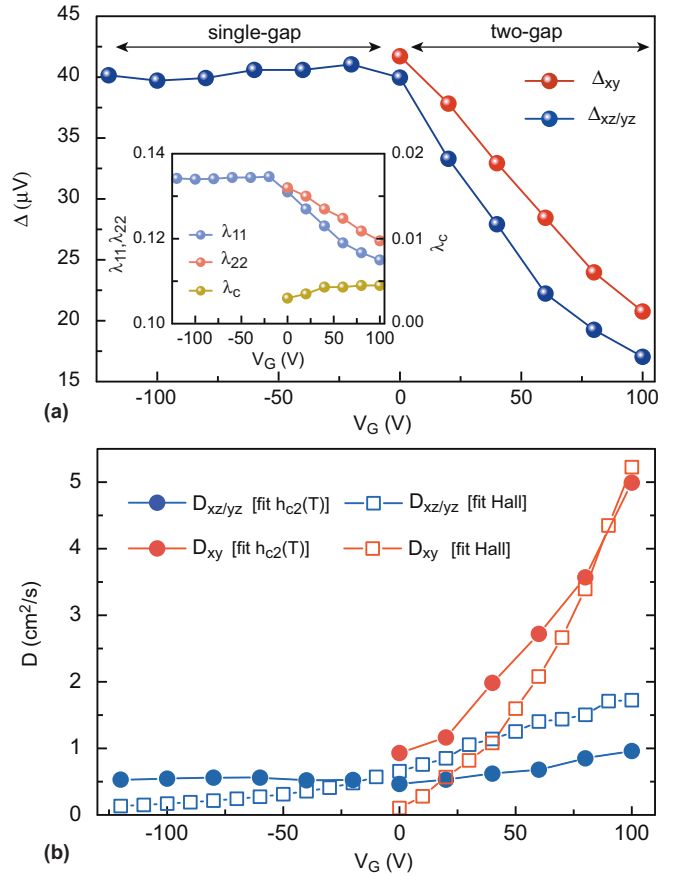


FIG. 4. (a) Evolution of the superconducting gap energies $\Delta_{xz,yz}$ and Δ_{xy} with gate voltage, extracted from the Usadel fitting procedure of $h_c(T)$ [Eq. (2)]. Inset: Intraband coupling constant $\lambda_{11(22)}$ (left axis) and average interband coupling constant $\lambda_c = \sqrt{\lambda_{12}\lambda_{21}}$ (right axis) extracted from the fits. (b) Diffusion constants in the two bands $D_{xz,yz}$ and D_{xy} , extracted from the fits and compared to the calculation derived from a two-band model analysis of the Hall effect (Appendix C).

IV. TWO-GAP S_{\pm} -WAVE SUPERCONDUCTIVITY DISORDER MODEL

The phase diagram in Fig. 1(e) shows a suppression of superconductivity in the two-gap regime, which is not expected within a simple Bardeen-Cooper-Schrieffer (BCS) approach since, at the Lifshitz transition, an increase in the number of electronic states available should enhance T_c . However, such weakening of superconductivity was predicted in multiband superconductors in the presence of disorder when the order parameters associated with each superconducting condensate have opposite sign because of a repulsive coupling ($\lambda_{12(21)} < 0$) [34,35,52]. In this situation, referred to as s_{\pm} -wave superconductivity, the suppression of T_c reflects a strong pair-breaking effect due to interband scattering. To describe quantitatively our experimental data, we developed a theoretical framework based on Golubov and Mazin's article for anisotropic multiband superconductors [34]. They showed that, in the presence of interband scattering, nonmagnetic impurities have a strong pair-breaking effect when the condensates have opposite signs. For s-wave superconductors,

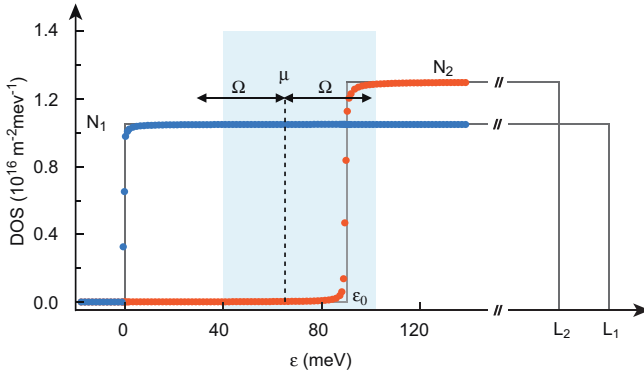


FIG. 5. Band structure considered in the two-band model. The solid grey lines show the clean case (no disorder), while the blue and red symbols show the dirty case for both bands, with an inverse scattering time $\tau^{-1} = 0.4$ meV. The shaded blue area corresponds to the experimental accessible chemical potential window.

this situation is analogous to single-band d -wave ones, and T_c decreases the same way when the scattering rate is increased. The BCS approach of Ref. [34] focuses on metallic three-dimensional (3D) systems having bands at half-filling with a large and constant density of state (DOS). Trevisan *et al.* adapted this calculation to oxide interfaces, introducing their 2D character, and the progressive filling of the bands by doping [35]. It is worth noticing that when the chemical potential μ reaches the second band upon doping [53], the energy difference with the bottom of the band is much lower than the energy of the superconducting glue Ω (the Debye energy in case of phonon-mediated superconductivity), leading to strongly coupled Cooper pairs as in the BEC limit.

We propose a realistic model based on the *experimentally* determined parameters and the two following ingredients: (i) we consider that the lower band is in the BCS limit, while the second one in the BEC one [53]; (ii) we take into account the broadening of the DOS by disorder in both bands, which smoothes the BEC character of the second one. A sketch of the band structure is shown in the inset of Fig. 5. We consider two bands with constant DOS, N_1 and N_2 . Indicating with w_j the thresholds of the two bands with respect to the chemical potential μ , and with Λ_j the top of the two bands, we have $w_1 = -\mu$, $w_2 = \varepsilon_0 - \mu$ and $\Lambda_i = L_i - \mu$ (L_i being the top of the corresponding band), where ε_0 is the energy difference between the bottoms of the two bands. Note that, while the gate voltage ranges from -120 V to $+100$ V, the corresponding μ varies approximately from 50 meV to 95 meV. We take the Debye frequency $\Omega = 34.5$ meV [54] and the ultraviolet cutoffs $\Lambda_{1,2} > 1$ eV. Then, in the gate voltage range of our experiments, the first band stays in the BCS regime, while the second band, even when it starts to be involved in superconductivity, remains in the BEC regime.

The critical temperature is extracted from the linearized equation for the superconducting gaps in the presence of disorder in the Born approximation ([34])

$$\begin{pmatrix} \Delta_1 \\ \Delta_2 \end{pmatrix} = \begin{pmatrix} \lambda_{11} & \lambda_{12} \\ \lambda_{21} & \lambda_{22} \end{pmatrix} \begin{pmatrix} A_{11} & A_{12} \\ A_{21} & A_{22} \end{pmatrix} \begin{pmatrix} \Delta_1 \\ \Delta_2 \end{pmatrix}, \quad (3)$$

where

$$A_{ij} = k_B T \sum_n \frac{M_{ij}}{\text{Det}(M)} \int_{v_i}^{\Xi_i} \frac{d\xi}{\tilde{\omega}_n^2 + (\xi + h_n)^2},$$

$v_i \equiv \text{Max}(-\Omega, w_i)$, $\Xi_i \equiv \text{Max}(\Omega, w_i)$, when $\mu \ll L_i$, $\tilde{\omega}_n$ and h_n are calculated self-consistently as

$$\tilde{\omega}_n = \omega_n + \frac{\tilde{\omega}_n}{4\tau} \sum_{j=1,2} f_{n,j},$$

$$h_n = -\frac{1}{4\tau} \sum_{j=1,2} g_{n,j}, \quad (4)$$

$\omega_n = (2n + 1)\pi k_B T$, are the Matsubara frequencies, $f_{n,j} = \frac{1}{\pi} \int_{w_j}^{\Lambda_j} \frac{d\xi}{\tilde{\omega}_n^2 + (\xi + h_n)^2}$, $g_{n,j} = \frac{1}{\pi} \int_{w_j}^{\Lambda_j} \frac{(\xi + h_n)d\xi}{\tilde{\omega}_n^2 + (\xi + h_n)^2}$, and

$$M = \begin{pmatrix} 1 - \frac{1}{4\tau} f_{n,1} & \frac{1}{4\tau} f_{n,1} \\ \frac{1}{4\tau} f_{n,2} & 1 - \frac{1}{4\tau} f_{n,2} \end{pmatrix}.$$

For simplicity, in this model we consider a single scattering time τ . Equation (4) displays the disorder-induced self-energy corrections to the Matsubara frequency and to the band energy, while the term $M/\text{Det}(M)$ in Eq. (3) enforces the disorder-induced vertex corrections to the coupling constants λ 's.

Finding the zero of the determinant of the homogeneous linear problem set by Eq. (3), we obtain T_c versus μ and, using the relation $n(\mu, T) = \int d\varepsilon [\tilde{N}_1(\varepsilon) + \tilde{N}_2(\varepsilon)] f(\varepsilon)$, where $\tilde{N}_{1,2}(\varepsilon)$ are the disorder-broadened DOS and $f(\varepsilon) = \{\exp[(\varepsilon - \mu)/k_B T] + 1\}^{-1}$ is the Fermi distribution function, together with the experimental relation $n_{2D}(V_G)$, we finally obtain T_c versus V_G . In order to map the chemical potential μ into the gate voltage V_G , we have to first calculate the correction to the DOS due to disorder by solving self-consistently the following equations:

$$\tilde{N}_i = \text{Im} \int_{w_i}^{\Lambda_i} \frac{N_i(\xi)}{\varepsilon - \xi - \Sigma_i} d\xi = N_i \text{Im}(\Sigma_i), \quad (5)$$

$$\Sigma_i(\varepsilon) = \sum_n \frac{\tau^{-1}}{2\pi} \ln \frac{\varepsilon - w_i - \Sigma_i}{\varepsilon - \Lambda_i - \Sigma_i},$$

$$\Sigma_i^{n=0} = i \frac{\tau^{-1}}{2\pi}. \quad (6)$$

Then the chemical potential μ is mapped into the number of particles following

$$n(\mu) = \sum_{i=1,2} \int_{-\infty}^{\mu} N_i(\xi) d\xi. \quad (7)$$

The DOS $N_1 = 1.05 \times 10^{16} \text{ m}^{-2} \text{ meV}^{-1}$ and $N_2 = 1.3 \times 10^{16} \text{ m}^{-2} \text{ meV}^{-1}$ are taken from angle-resolved photoemission spectroscopy (ARPES) studies on (110)-oriented SrTiO₃ crystals [55]. We assume that the interband superconducting coupling constants are independent of doping and take the experimental values $\lambda_{11} = 0.135$ and $\lambda_{22} = 0.14$ at the Lifshitz transition. For the interband coupling, we take $\lambda_{12} = \lambda_{21} \cdot N_2/N_1 = \pm \lambda_{11}/10$, which leads to a λ_c a bit larger than that determined through Usadel fits as expected since the second band is in the BEC limit (+ and - signs refer respectively to attractive and repulsive interband pairing).

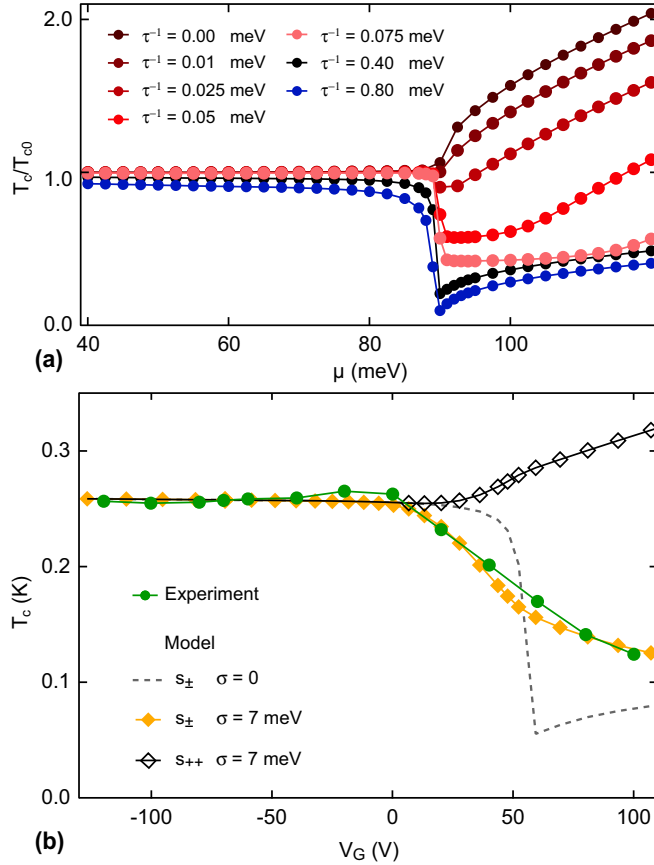


FIG. 6. (a) Calculated T_c normalized to the bare single-band superconducting critical temperature T_{c0} in the clean limit, as a function of the chemical potential μ for different scattering rates τ^{-1} in the repulsive interband pairing case (s_{\pm}). (b) Experimental (green circles) and calculated superconducting T_c as a function of the gate voltage V_G both in the case of attractive (black diamonds) and repulsive (orange diamonds) interband coupling, with the variance of the chemical potential disorder $\sigma = 7$ meV and $\tau^{-1} = 0.4$ meV. Dashed line shows the computed curve in absence of mesoscale disorder in the s_{\pm} scenario ($\sigma = 0$ meV).

The scattering rate τ^{-1} is a key ingredient, which first sets the depairing effect by band mixing and second, makes the BEC effect more visible. From transport measurements, we estimate an upper bound value of $\tau^{-1} = 0.4$ meV that we keep constant (Appendix C). Figure 6(a) shows the evolution of T_c with the chemical potential μ in the repulsive case for different scattering rates, assuming $\varepsilon_0 \approx 90$ meV. The dramatic drop of T_c at the Lifshitz transition is enhanced for increasing τ^{-1} . The “V-shaped” curve is characteristic of the BEC scenario.

In Fig. 6(b), we compare the experimental data (green symbols) with the gate evolution of T_c calculated in the repulsive case (dashed line). The two overlap quantitatively up to $V_G \simeq 0$ V, but the V-shape well is not seen in the data. The agreement between our theoretical results and the experimental data is further improved considering small fluctuations of the local chemical potential due to mesoscale disorder at SrTiO₃-based

interfaces as already widely documented [56–61]. We therefore consider the average value

$$\bar{T}_c(\mu) = \frac{1}{\sigma} \int_{-\infty}^{+\infty} d\mu' T_c(\mu') G\left(\frac{\mu' - \mu}{\sigma}\right),$$

where G is a standard Gaussian distribution, μ is the average value of the chemical potential, and σ is its variance. A good agreement with experimental data is obtained for $\sigma = 7$ meV [solid diamonds symbols in Fig. 6(b)]. Unfortunately, this prevents us from clearly seeing the occurrence of the BEC-BCS cross-over in this system. The very same calculation using an attractive interband pairing constant cannot reproduce the experimental data [s_{++} -wave case in Fig. 6(b)]. Our analysis clearly supports a s_{\pm} -wave multigap superconductivity in the overdoped regime of (110)-oriented LaAlO₃/SrTiO₃ interfaces.

V. CONCLUSION

In summary, our results demonstrate that multicondensate superconductivity can take place in doped SrTiO₃ as suggested by the seminal experiment of Binnig *et al.*. The (110)-orientated LaAlO₃/SrTiO₃ interface considered in this work is an ideal system since its interfacial quantum well accommodates two bands of rather large DOS, sufficiently decoupled in the k -space and real space to give rise to an observable two-gap superconductivity. This is in contrast to the more conventional (001)-oriented LaAlO₃/SrTiO₃ for which experiments are more consistent with single-gap superconductivity. In this case, the weak DOS of the low-energy d_{xy} bands preclude the formation of superconductivity at low doping and single gap superconductivity only occurs when the high DOS $d_{xz/yz}$ band is populated. However, a recent work suggested that the decrease of T_c in the high-doping regime of (001)-oriented LaAlO₃/SrTiO₃ interfaces could also be due to the formation of a s_{\pm} -superconducting state when a high-energy replica of the d_{xy} band starts to be filled [62]. This is supported by recent experiments on LaAlO₃/SrTiO₃ junctions which demonstrated the presence of π -shift Josephson channels, consistent with the formation of such a state in this system [63]. The presence of a repulsive coupling between the two condensates has strong implications on the possible origin of superconductivity in SrTiO₃, which has been attributed to a variety of mechanisms, including plasmon-mediated pairing [22], ferroelectric fluctuations [20,64,65], and polar optical phonons [21].

ACKNOWLEDGMENTS

This work was supported by the ANR PRC (QUANTOP), by the QuantERA ERA-NET Cofund in Quantum Technologies (Grant Agreement No. 731473) implemented within the European Union’s Horizon 2020 Program (QUANTOX) and the Île de France SESAME program, by the PID2020-118479RB-I00, PID2020-112548RB-I00 and Severo Ochoa FUNFUTURE (CEX2019-000917-S) projects of the Spanish Ministry of Science and Innovation (MCIN/AEI/10.13039/501100011033), by the Generalitat de Catalunya (2017 SGR 1377), by Sapienza Università di Roma, through the projects, Ateneo 2018

(Grant No. RM11816431DBA5AF), Ateneo 2019 (Grant No. RM11916B56802AFE), Ateneo 2020 (Grant No. RM120172A8CC7CC7), and by the Italian Ministero dell'Istruzione, dell'Università e della Ricerca, through the Project No. PRIN 2017Z8TS5B. G.S. acknowledges financial support from the Beatriu de Pinós Programme and the Ministry of Research and Universities of the Government of Catalonia, with research Grant No. 2019 BP 00207.

APPENDIX A: TWO-CARRIER ANALYSIS OF HALL EFFECT AND GATE CAPACITANCE MEASUREMENTS

A two-carrier analysis of R_{Hall} versus field for different gate voltages V_G gives access to the carrier densities and mobilities in the entire phase diagram, providing the variation of the total carrier density in the gate voltage range is known. The gate evolution of the total carrier density with gate voltage can be retrieved from the integral of the gate capacitance $C(V_G)$ [37], as

$$n_{2D}(V_G) = n_{2D}(V_G = -120 \text{ V}) + \frac{1}{eA} \int_{-120 \text{ V}}^{V_G} C(V) dV, \quad (\text{A1})$$

where A is the area of the sample and e is the elementary charge. Here $C(V_G)$ was determined from the complex impedance measurement of the gate capacitor $Z(\omega) = \frac{1}{jC\omega}$ as a function of gate voltage. The value $n_{2D}(V_G = -120 \text{ V})$ is matched to $n_{\text{Hall}} = \frac{B}{eR_{\text{Hall}}}$ for $V_G = -120 \text{ V}$ in the single-band regime. In the multiband transport regime (for $V_G \gtrsim 0 \text{ V}$), the Hall resistance has been fitted with a two-band model, Eq. (A2), corresponding to two populations of electrons (density $n_{1(2)}$, mobility $\mu_{1(2)}$),

$$R_{\text{Hall}} = \frac{H}{e} \frac{\frac{n_1 \mu_1^2}{1 + \mu_1^2 H^2} + \frac{n_2 \mu_2^2}{1 + \mu_2^2 H^2}}{\left[\frac{n_1 \mu_1}{1 + \mu_1^2 H^2} + \frac{n_2 \mu_2}{1 + \mu_2^2 H^2} \right]^2 + \left[\frac{n_1 \mu_1^2 H}{1 + \mu_1^2 H^2} + \frac{n_2 \mu_2^2 H}{1 + \mu_2^2 H^2} \right]^2}, \quad (\text{A2})$$

where $n_1 + n_2 = n_{2D}$. The results of the fitting procedure are shown in Fig. 7 (densities only). For $V_G \gtrsim 0 \text{ V}$, the majority of electrons has a low mobility $\mu_{\text{LM}} \approx 100 \text{ cm}^2/(\text{V} \times \text{s})$. These electrons are associated to the $d_{xz,yz}$ band. A second population of high-mobility electrons (μ_{HM}) representing less than 10% of the total carrier density emerges around $V_G \simeq 0 \text{ V}$ and is associated to the higher-energy d_{xy} band.

APPENDIX B: SUPERCONDUCTING GAP CALCULATION

For a two-gap superconductor, the gaps $\Delta_{v=1,2}$ can be deduced from the coupling constants by solving self-consistently the two following equations [66]:

$$\Delta_v = \sum_{\mu=1,2} \lambda_{v\mu} \Delta_{\mu} \left(\frac{1}{\tilde{\lambda}} + \ln \frac{T_c}{T} - A_{\mu} \right), \quad (\text{B1})$$

$$A_{\mu} = \sum_{n=0}^{\infty} \left(\frac{1}{n + \frac{1}{2}} - \frac{1}{\sqrt{\left(\frac{\Delta_{\mu}}{2\pi k_B T} \right)^2 + \left(n + \frac{1}{2} \right)^2}} \right), \quad (\text{B2})$$

where $\tilde{\lambda} = \frac{2(\lambda_{11}\lambda_{22} - \lambda_{12}\lambda_{21})}{\lambda_{11} + \lambda_{22} - \sqrt{(\lambda_{11}\lambda_{22})^2 + 4\lambda_{12}\lambda_{21}}}$. The superconducting critical temperature is given by $T_c \simeq 1.14T_D \exp(-\frac{1}{\tilde{\lambda}})$.

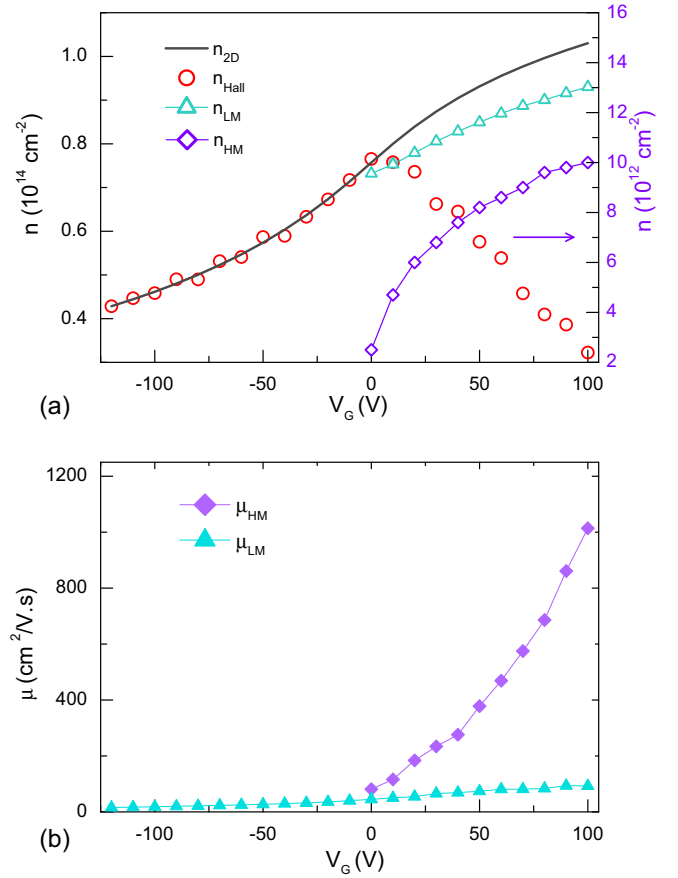


FIG. 7. (a) Gate voltage dependence of the carrier density of the low-mobility n_{LM} and high-mobility n_{HM} population of electrons extracted from the two-carrier analysis of the Hall effect at $T = 3 \text{ K}$. Red circles indicate the Hall carrier density measured in the limit of zero-magnetic field, $n_{\text{Hall}}(B \rightarrow 0)$, which only gives the correct electron density in the single band regime, i.e., for $V_G \lesssim 0 \text{ V}$. The total carrier density of the 2-DEG n_{2D} was obtained by integration of the gate capacitance and by matching it to n_{Hall} in the one-band regime [Eq. (8)]. (b) Mobility of the less mobile carriers μ_{LM} and the more mobile ones μ_{HM} as a function of the gate voltage.

APPENDIX C: DIFFUSION CONSTANTS

In Fig. 4(b) of the article, we show the evolution of the diffusion constants $D_1 = D_{xz/yz}$ and $D_2 = D_{xy}$ with gate voltage extracted from the Usadel fits of $H_{c2}(T)$ curves, Eq. (2). While $D_{xz/yz}$ only weakly evolves with gate voltage, D_{xy} strongly increases in the two-band regime as already noticed in the gate dependence of the mobility. Using the two-band model presented above we extracted the carrier density and scattering time associated with each band in a simple Drude picture and evaluated the corresponding diffusion constant $D_{1(2)} = \frac{1}{3} v_{F1(2)}^2 \tau_{1(2)}$ (subscripts 1 and 2 refer to the $d_{xz,yz}$ and d_{xy} bands, respectively). $\tau_{1,2} = \frac{1}{e} m_{1,2}^* \mu_{1,2}$ is the Drude elastic time. Assuming parabolic bands the Fermi velocity is given by $v_{F1,2} = \frac{\hbar k_{F1,2}}{m_{1,2}^*}$ where $k_{F1,2} = \sqrt{2\pi n_{1,2}}$ is the Fermi wave vector. As seen in Fig. 3(b) of the main text, the diffusion constants calculated with this crude approach reproduces qualitatively that extracted from Usadel fits, in particular, the strong increase of D_{xy} with gate voltage, taking in-plane effective

masses $m_1^* \approx 2$ and $m_2^* \approx 3$. These values are reasonably consistent with data in the literature [55]. From these data, we can compute the scattering rates τ_1^{-1} and τ_2^{-1} corresponding to the above-mentioned diffusion constants D_1 and D_2 . In the single-band regime, τ_{11}^{-1} can be unambiguously calculated ($\tau_1^{-1} = \tau_{11}^{-1}$). In the two-band regime, the situation is more complex with intraband $\tau_{11(22)}^{-1}$ and interband $\tau_{12(21)}^{-1}$ scattering rates. The diffusion constants we can extract from the Usadel fits of the data are combinations of these individual scattering rates. Given the additivity of the scattering rates, we know that

individual scattering rates are smaller than the τ_i^{-1} ($i = 1, 2$) we extracted from the Usadel fit. For instance, in the second band, $\tau_{22}^{-1} < \tau_2^{-1}$ and $\tau_{12}^{-1} < \tau_2^{-1}$. The most relevant scattering rate is the interband one (τ_{12}^{-1}) that mainly controls the depairing effect. We can estimate its maximum value by taking the minimum value of τ_2^{-1} . The highest diffusion constant value reported in Fig. 4(b) of the article is $\approx 5 \text{ cm}^2/\text{Vs}^{-1}$, corresponding to the scattering rate expressed in scattering energy $\tau_2^{-1} \sim 0.4 \text{ meV}$. As a consequence, this is the maximum value of τ_{12}^{-1} and in our model we will take $\tau^{-1} = 0.4 \text{ meV}$.

-
- [1] I. I. Mazin, D. J. Singh, M. D. Johannes, and M. H. Du, *Phys. Rev. Lett.* **101**, 057003 (2008).
- [2] F. Wang and D.-H. Lee, *Science* **332**, 200 (2011).
- [3] P. J. Hirschfeld, M. M. Korshunov, and I. I. Mazin, *Rep. Prog. Phys.* **74**, 124508 (2011).
- [4] Y. Asano, A. Sasaki, and A. A. Golubov, *New J. Phys.* **20**, 043020 (2018).
- [5] M. S. Scheurer and J. Schmalian, *Nat. Commun.* **6**, 6005 (2015).
- [6] F. Giubileo, D. Roditchev, W. Sacks, R. Lamy, D. X. Thanh, J. Klein, S. Miraglia, D. Fruchart, J. Marcus, and Ph. Monod, *Phys. Rev. Lett.* **87**, 177008 (2001).
- [7] L. Shan, Y.-L. Wang, B. Shen, B. Zeng, Y. Huang, A. Li, D. Wang, H. Yang, C. Ren, Q.-H. Wang, S. H. Pan, and H.-H. Wen, *Nat. Phys.* **7**, 325 (2011).
- [8] M. L. Teague, G. K. Drayna, G. P. Lockhart, P. Cheng, B. Shen, H.-H. Wen, and N.-C. Yeh, *Phys. Rev. Lett.* **106**, 087004 (2011).
- [9] T. Hanaguri, S. Niitaka, K. Kuroki, and H. Takagi, *Science* **328**, 474 (2010).
- [10] P. O. Sprau, A. Kostin, A. Kreisel, A. E. Böhmer, V. Taufour, P. C. Canfield, S. Mukherjee, P. J. Hirschfeld, B. M. Andersen, and J. C. Samus Davis, *Science* **357**, 75 (2017).
- [11] G. Seyfarth, J.-P. Brison, M.-A. Méasson, J. Flouquet, K. Izawa, Y. Matsuda, H. Sugawara, and H. Sato, *Phys. Rev. Lett.* **95**, 107004 (2005).
- [12] S. Kittaka, Y. Aoki, Y. Shimura, T. Sakakibara, S. Seiro, C. Geibel, F. Steglich, H. Ikeda, and K. Machida, *Phys. Rev. Lett.* **112**, 067002 (2014).
- [13] J. F. Schooley, W. R. Hosler, and M. L. Cohen, *Phys. Rev. Lett.* **12**, 474 (1964).
- [14] X. Lin, G. Bridoux, A. Gourgout, G. Seyfarth, S. Krämer, M. Nardone, B. Fauqué, and K. Behnia, *Phys. Rev. Lett.* **112**, 207002 (2014).
- [15] G. Binnig, A. Baratoff, H. E. Hoenig, and J. G. Bednorz, *Phys. Rev. Lett.* **45**, 1352 (1980).
- [16] A. G. Swartz, H. Inoue, T. A. Merz, Y. Hikita, S. Raghu, T. P. Devereaux, S. Johnstone, and H. Y. Hwang, *Proc. Natl. Acad. Sci. U.S.A.* **115**, 1475 (2018).
- [17] M. Thiemann, M. H. Beutel, M. Dressel, N. R. Lee-Hone, D. M. Broun, E. Fillis-Tsirakis, H. Boschker, J. Mannhart, and M. Scheffler, *Phys. Rev. Lett.* **120**, 237002 (2018).
- [18] N. Reyren, S. Thiel, A. D. Caviglia, L. Fitting Kourkoutis, G. Hammerl, C. Richter, C. W. Schneider, T. Kopp, A.-S. Ruetschi, D. Jaccard, M. Gabay, D. A. Muller, J.-M. Triscone, and J. Mannhart, *Science* **317**, 1196 (2007).
- [19] J. Biscaras, N. Bergeal, A. Kushwaha, T. Wolf, A. Rastogi, R. C. Budhani, and J. Lesueur, *Nat. Commun.* **1**, 89 (2010).
- [20] J. M. Edge, Y. Kedem, U. Aschauer, N. A. Spaldin, and A. V. Balatsky, *Phys. Rev. Lett.* **115**, 247002 (2015).
- [21] L. P. Gorkov, *Proc. Natl. Acad. Sci. U.S.A.* **113**, 4646 (2016).
- [22] J. Ruhman and P. A. Lee, *Phys. Rev. B* **94**, 224515 (2016).
- [23] Z. S. Popovic, S. Satpathy, and R. M. Martin, *Phys. Rev. Lett.* **101**, 256801 (2008).
- [24] P. Delugas, A. Filippetti, V. Fiorentini, D. I. Bilc, D. Fontaine, and P. Ghosez, *Phys. Rev. Lett.* **106**, 166807 (2011).
- [25] N. Scopigno, D. Bucheli, S. Caprara, J. Biscaras, N. Bergeal, J. Lesueur, and M. Grilli, *Phys. Rev. Lett.* **116**, 026804 (2016).
- [26] M. Salluzzo, J. C. Cezar, N. B. Brookes, V. Bisogni, G. M. De Luca, C. Richter, S. Thiel, J. Mannhart, M. Huijben, A. Brinkman, G. Rijnders, and G. Ghiringhelli, *Phys. Rev. Lett.* **102**, 166804 (2009).
- [27] D. Pesquera, M. Scigaj, P. Gargiani, A. Barla, J. Herrero-Martín, E. Pellegrin, S. M. Valvidares, J. Gázquez, M. Varela, N. Dix, J. Fontcuberta, F. Sánchez, and G. Herranz, *Phys. Rev. Lett.* **113**, 156802 (2014).
- [28] G. M. De Luca, R. Di Capua, E. Di Gennaro, A. Sambri, F. M. Granozio, G. Ghiringhelli, D. Betto, C. Piamonteze, N. B. Brookes, and M. Salluzzo, *Phys. Rev. B* **98**, 115143 (2018).
- [29] A. M. R. V. L. Monteiro, M. Vivek, D. J. Groenendijk, P. Bruneel, I. Leermakers, U. Zeitler, M. Gabay, and A. D. Caviglia, *Phys. Rev. B* **99**, 201102(R) (2019).
- [30] A. Annadi, Q. Zhang, X. Renshaw Wang, N. Tuzla, K. Gopinadhan, W. M. Lü, A. Roy Barman, Z. Q. Liu, A. Srivastava, S. Saha, Y. L. Zhao, S. W. Zeng, S. Dhar, E. Olsson, B. Gu, S. Yunoki, S. Maekawa, H. Hilgenkamp, T. Venkatesan, and Ariando, *Nat. Commun.* **4**, 1838 (2013).
- [31] A. D. Caviglia, S. Gariglio, N. Reyren, D. Jaccard, T. Schneider, M. Gabay, S. Thiel, G. Hammerl, J. Mannhart, and J.-M. Triscone, *Nature* **456**, 624 (2008).
- [32] J. Biscaras, N. Bergeal, S. Hurand, C. Grossetete, A. Rastogi, R. C. Budhani, D. LeBoeuf, C. Proust, and J. Lesueur, *Phys. Rev. Lett.* **108**, 247004 (2012).
- [33] G. Herranz, G. Singh, N. Bergeal, A. Jouan, J. Lesueur, J. Gázquez, M. Varela, M. Scigaj, N. Dix, F. Sánchez, and J. Fontcuberta, *Nat. Commun.* **6**, 6028 (2015).
- [34] A. A. Golubov and I. I. Mazin, *Phys. Rev. B* **55**, 15146 (1997).
- [35] T. V. Trevisan, M. Schütt, and R. M. Fernandes, *Phys. Rev. Lett.* **121**, 127002 (2018).
- [36] J. Biscaras, S. Hurand, C. Feuillet-Palma, A. Rastogi, R. C. Budhani, N. Reyren, E. Lesne, J. Lesueur, and N. Bergeal, *Sci. Rep.* **4**, 6788 (2014).

- [37] G. Singh, A. Jouan, S. Hurand, C. Feuillet-Palma, P. Kumar, A. Dogra, R. Budhani, J. Lesueur, and N. Bergeal, *Phys. Rev. B* **96**, 024509 (2017).
- [38] N. R. Werthamer, E. Helfand, and P. C. Hohenberg, *Phys. Rev.* **147**, 295 (1966).
- [39] M. Palistrant, A. Surdu, V. Ursu, P. Petrenko, and A. Sidorenko, *Low Temp. Phys.* **37**, 451 (2011).
- [40] F. Hunte, J. Jaroszynski, A. Gurevich, D. C. Larbalestier, R. Jin, A. S. Sefat, M. A. McGuire, B. C. Sales, D. K. Christen, and D. Mandrus, *Nature* **453**, 903 (2008).
- [41] M. A. Zehetmayer, *Supercond. Sci. Technol.* **26**, 043001 (2013).
- [42] J. A. Bert, K. C. Nowack, B. Kalisky, H. Noad, J. R. Kirtley, C. Bell, H. K. Sato, M. Hosoda, Y. Hikita, H. Y. Hwang, and K. A. Moler, *Phys. Rev. B* **86**, 060503(R) (2012).
- [43] G. Singh, A. Jouan, L. Benfatto, F. Couëdo, P. Kumar, A. Dogra, R. C. Budhani, S. Caprara, M. Grilli, E. Lesne, A. Barthélémy, M. Bibes, C. Feuillet-Palma, J. Lesueur, and N. Bergeal, *Nat. Commun.* **9**, 407 (2018).
- [44] C. Richter, H. Boschker, W. Dietsche, E. Fillis-Tsirakis, R. Jany, F. Loder, L. F. Kourkoutis, D. A. Muller, J. R. Kirtley, C. W. Schneider, and J. Mannhart, *Nature* **502**, 528 (2013).
- [45] D. Bucheli, M. Grilli, F. Peronaci, G. Seibold, and S. Caprara, *Phys. Rev. B* **89**, 195448 (2014).
- [46] A. D. Caviglia, M. Gabay, S. Gariglio, N. Reyren, C. Cancellieri, and J.-M. Triscone, *Phys. Rev. Lett.* **104**, 126803 (2010).
- [47] M. Ben Shalom, C. W. Tai, Y. Lereah, M. Sachs, E. Levy, D. Rakhmilevitch, A. Palevski, and Y. Dagan, *Phys. Rev. B* **80**, 140403(R) (2009).
- [48] L. P. Gorkov and E. I. Rashba, *Phys. Rev. Lett.* **87**, 037004 (2001).
- [49] G. Singh, A. Jouan, G. Herranz, M. Scigaj, F. Sánchez, L. Benfatto, S. Caprara, M. Grilli, G. Saiz, F. Couëdo, C. Feuillet-Palma, J. Lesueur, and N. Bergeal, *Nat. Mater.* **18**, 948 (2019).
- [50] R. M. Fernandes, J. T. Haraldsen, P. Wölfle, and A. V. Balatsky, *Phys. Rev. B* **87**, 014510 (2013).
- [51] A. Gurevich, *Phys. Rev. B* **67**, 184515 (2003).
- [52] V. G. Kogan and R. Prozorov, *Phys. Rev. B* **93**, 224515 (2016).
- [53] This is not the case for the first band since the Fermi energy is on the order of 100 meV, the distance between the bottom of the two bands is 90 meV, and the characteristic frequency $\Omega = 34.5$ meV [54]. In the accessible experimental doping regime, the BEC-like situation occurs only when the second band starts to be filled, contrary to the Trevisan *et al.* calculation [35], where both bands are in the BEC limit.
- [54] E. Maniv, M. Ben Shalom, A. Ron, M. Mograbi, A. Palevski, M. Goldstein, and Y. Dagan, *Nat. Commun.* **6**, 8239 (2015).
- [55] Z. Wang, Z. Zhong, X. Hao, S. Gerhold, B. Stöger, M. Schmid, J. Sánchez-Barriga, A. Varykhalov, C. Franchini, K. Held, and U. Diebold, *Proc. Natl. Acad. Sci. U.S.A.* **111**, 3933 (2014).
- [56] J. Biscaras, N. Bergeal, S. Hurand, C. Feuillet-Palma, A. Rastogi, R. C. Budhani, M. Grilli, S. Caprara, and J. Lesueur, *Nat. Mater.* **12**, 542 (2013).
- [57] D. Bucheli, S. Caprara, C. Castellani, and M. Grilli, *New J. Phys.* **15**, 023014 (2013).
- [58] S. Caprara, J. Biscaras, N. Bergeal, D. Bucheli, S. Hurand, C. Feuillet-Palma, A. Rastogi, R. C. Budhani, J. Lesueur, and M. Grilli, *Phys. Rev. B* **88**, 020504(R) (2013).
- [59] G. Dezi, N. Scopigno, S. Caprara, and M. Grilli, *Phys. Rev. B* **98**, 214507 (2018).
- [60] S. Hurand, A. Jouan, E. Lesne, G. Singh, C. Feuillet-Palma, M. Bibes, A. Barthélémy, J. Lesueur, and N. Bergeal, *Phys. Rev. B* **99**, 104515 (2019).
- [61] G. Venditti, J. Biscaras, S. Hurand, N. Bergeal, J. Lesueur, A. Dogra, R. C. Budhani, M. Mondal, J. Jesudasan, P. Raychaudhuri, S. Caprara, and L. Benfatto, *Phys. Rev. B* **100**, 064506 (2019).
- [62] A. Jouan, S. Hurand, G. Singh, E. Lesne, A. Barthelemy, M. Bibes, C. Ulysse, G. Saiz, C. Feuillet-Palma, J. Lesueur, and N. Bergeal, [arXiv:2104.08220](https://arxiv.org/abs/2104.08220).
- [63] G. Singh, C. Guarcello, E. Lesne, D. Winkler, T. Claeson, T. Bauch, F. Lombardi, A. D. Caviglia, R. Citro, Ma. Cuoco, and A. Kalaboukhov, *npj Quantum Mater.* **7**, 2 (2022).
- [64] J. R. Arce-Gamboa and G. G. Guzmán-Verri, *Phys. Rev. Materials* **2**, 104804 (2018).
- [65] S. E. Rowley, L. J. Spalek, R. P. Smith, M. P. M. Dean, M. Itoh, J. F. Scott, G. G. Lonzarich, and S. S. Saxena, *Nat. Phys.* **10**, 367 (2014).
- [66] V. G. Kogan, C. Martin, and R. Prozorov, *Phys. Rev. B* **80**, 014507 (2009).